HHS Public Access

Author manuscript

J Struct Biol. Author manuscript; available in PMC 2022 March 01.

Published in final edited form as:

J Struct Biol. 2021 March ; 213(1): 107681. doi:10.1016/j.jsb.2020.107681.

Structural Analysis of Histone Deacetylase 8 Mutants Associated with Cornelia de Lange Syndrome Spectrum Disorders

Jeremy D. Osko[a,1], **Nicholas J. Porter**[a,2], **Christophe Decroos**[a,3], **Matthew S. Lee**[a,4], **Paris R. Watson**[a], **Sarah E. Raible**[b], **Ian D. Krantz**[b,c], **Matthew A. Deardorff**[d], **David W. Christianson**[a,*]

[a]Roy and Diana Vagelos Laboratories, Department of Chemistry, University of Pennsylvania, 231 South 34th Street, Philadelphia, PA 19104-6323, United States

[b]Roberts Individualized Medical Genetics Center, Division of Human Genetics, The Children's Hospital of Philadelphia, Philadelphia, PA 19104, United States

[c]Department of Pediatrics, University of Pennsylvania Perelman School of Medicine, Philadelphia, PA 19104, United States

[d]Departments of Pathology and Pediatrics, Children's Hospital Los Angeles and the Keck School of Medicine of the University of Southern California, Los Angeles, CA 90033, United States

Abstract

Cornelia de Lange Syndrome (CdLS) and associated spectrum disorders are characterized by one or more congenital anomalies including distinctive facial features, upper limb abnormalities, intellectual disability, and other symptoms. The molecular genetic basis of CdLS is linked to defects in cohesin, a protein complex that functions in sister chromatid cohesion, chromatin organization, and transcriptional regulation. Histone deacetylase 8 (HDAC8) plays an important role in cohesin function by catalyzing the deacetylation of SMC3, which is required for efficient recycling of the cohesin complex. Missense mutations in HDAC8 have been identified in children diagnosed with CdLS spectrum disorders, and here we outline structure-function relationships for four of these mutations. Specifically, we report the 1.50 Å-resolution structure of the I45T HDAC8–suberoylanilide hydroxamic acid complex, the 1.84 Å-resolution structure of E66D/Y306F HDAC8 complexed with a peptide assay substrate, and the 2.40 Å-resolution structure of G320R HDAC8 complexed with the inhibitor M344. Additionally, we present a computationally generated model of D176G HDAC8. These structures illuminate new structure-function relationships for HDAC8 and highlight the importance of long-range interactions in the protein scaffold that can influence catalytic function.

*author to whom correspondence should be sent: chris@sas.upenn.edu.

[1]Current address: Department of Molecular Biology, Princeton University, Princeton, NJ 08544-1014, United States

[2]Current address: Division of Chemistry and Chemical Engineering, California Institute of Technology, 1200 East California Boulevard, Pasadena, CA 91125, United States

[3]Current address: Aix Marseille Univ, CNRS, Centrale Marseille, iSm2, Marseille, France

[4]Current address: Carle Illinois College of Medicine, University of Illinois at Urbana-Champaign, Champaign, IL 61820, United States

Keywords

X-ray crystallography; zinc enzyme; cohesin; birth defect

1. Introduction

First described more than a century ago (Brachmann, 1916; De Lange, 1933, 1938), Cornelia de Lange Syndrome (CdLS) and associated spectrum disorders are characterized by one or more congenital anomalies including distinctive facial features, but also including upper limb abnormalities, compromised organ function, intellectual disability, and other symptoms (Kline et al., 2018; Deardorff et al., 2020). The CdLS phenotype is often recognizable at birth due to distinctive craniofacial dysmorphism that can be diagnosed through computational analysis (Loos et al., 2003; Rohatgi et al., 2010; Dowsett et al., 2018; Gurovich et al., 2019). However, such features can vary widely, and not all children diagnosed with CdLS present with the classic phenotype (Kline et al., 2018).

The majority of children diagnosed with CdLS spectrum disorders have defects in genes encoding cohesin proteins or proteins that enable proper cohesin function. The molecular etiology of CdLS is thus rooted in dysfunction of the cohesin complex that encircles sister chromatids during cell division, regulates chromatin function, and regulates transcription (Boyle et al., 2015; Hons et al., 2016; Izumi et al., 2016; Kline et al., 2018; Sarogni et al., 2019; Shi et al., 2020). Gene identification efforts have revealed that the majority of CdLS patients carry a mutation in genes encoding the cohesin structural proteins SMC1A, SMC3, and RAD21, as well as the regulatory proteins NIPBL and the deacetylase HDAC8 (Deardorff et al., 2012; Kaiser et al., 2014; Feng et al., 2014; Parenti et al., 2016; Yuan et al., 2019).

Current models for the function of HDAC8 implicate it in cohesin recycling. Cohesin is thought to encircle sister chromatids (Gruber et al., 2003), with core proteins SMC1A and SMC3 linked at one end by a “hinge”, much like the two half-rings of a bracelet, and with RAD21 serving as the “clasp” of the bracelet (Figure 1A) (Deardorff et al., 2016).

The human cohesin protein SMC3 is acetylated at K105 and K106 following DNA replication during S phase, which locks sister chromatids together. Following cohesin removal and sister chromatid separation, deacetylation of K105 and K106 is thought to enable cohesin recycling. The discovery of HDAC8 mutations in children diagnosed with CdLS served to clarify the role of HDAC8 as the SMC3 deacetylase that enables cohesin recycling (Deardorff et al., 2012; Kaiser et al., 2014).

In previous studies, we have described structure-function studies of several CdLS HDAC8 mutations (Decroos et al., 2014; Decroos et al., 2015). Consistent with loss of HDAC8 function in cohesin recycling, deacetylase activity and/or thermostability is compromised in most CdLS HDAC8 mutants studied. In these studies, we have also identified that several mutations exhibiting diminished catalytic activity can be rescued by the small molecule activator N-(phenylcarbamothioyl)-benzamide. However, only mutations with modestly diminished reaction kinetics respond to this molecular activator.

Here, we report the X-ray crystal structures of two newly identified CdLS HDAC8 mutations, I45T and E66D. Specifically, we report the 1.50 Å-resolution structure of the complex between I45T HDAC8 and the inhibitor suberoylanilide hydroxamic acid (SAHA), and the 1.84 Å-resolution structure of the complex between E66D/Y306F HDAC8 and the assay substrate Ac-RHK$_{Ac}$K$_{Ac}$-AMC (Ac = acetyl, K$_{ac}$ = acetyllysine, AMC = aminomethylcoumarin). Additionally, we report the 2.40 Å-resolution structure of G320R HDAC8 (Kaiser et al., 2014) complexed with the hydroxamic acid-based inhibitor M344. Lastly, we present a model of the novel mutation D176G HDAC8 based on the recently reported structure of D176A HDAC8 (Gantt et al., 2016). The locations of I45T, E66D, D176G, and G320R in the HDAC8 structure are shown in Figure 1B. These studies extend our understanding of the molecular etiology of CdLS spectrum disorders as manifest in site-specific mutants of HDAC8 identified in the clinic.

2. Results

2.1. Catalytic activity of CdLS HDAC8 mutants

For recombinant wild-type HDAC8, the catalytic efficiency $k_{cat}/K_M = 2200 \pm 400\ M^{-1}\ s^{-1}$. In comparison, however, CdLS HDAC8 mutants I45T, E66D, and G320R exhibit catalytic efficiencies that are reduced to 15–20% of that measured for the wild-type enzyme (Table 1). We were unable to express D176G HDAC8, so we used the previously determined steady-state kinetic parameters of D176A HDAC8 as reasonable surrogates (Gantt et al., 2016). This mutant exhibits a 2800-fold reduction in catalytic efficiency. The deleterious effect of mutations is predominantly manifest in k_{cat}, which exhibits approximately 10–20-fold reductions, or in the case of D176A HDAC8, a 5400-fold reduction in k_{cat}. Increases in K_M for all mutants except D176A HDAC8 range only 2–5-fold compared with the wild-type enzyme; for D176A HDAC8, K_M decreases two-fold. Presuming that K_M represents the dissociation constant of the enzyme-substrate complex (Gantt et al., 2006), the minor effect of each mutation on K_M suggests that substrate binding is not substantially perturbed by any of the CdLS HDAC8 mutations studied.

2.2. Structure of the I45T HDAC8–SAHA complex

The I45T HDAC8 mutant was identified by three of us (M.A.D., I.D.K., S.E.R.) in a boy with small stature, mild intellectual disability, and mild facial features consistent with CdLS. The I45T mutation was inherited from his mother who had small stature, but was otherwise unaffected. The Cα atom of I45 is 22 Å away from the active site Zn^{2+} ion.

The I45T HDAC8–SAHA complex crystallizes in monoclinic space group $P2_1$ and contains two monomers in the asymmetric unit; crystals diffract to 1.50 Å resolution. There are no major conformational differences between I45T HDAC8 and the wild-type enzyme (PDB 1T69) (Somoza et al., 2004), and the root-mean-square deviation (rmsd) is 0.35 Å for 307 Cα atoms. The ionized hydroxamate group of SAHA chelates the catalytic Zn^{2+} ion through the N–O^- and C=O groups with bidentate coordination geometry (Figure 2). Additionally, the hydroxamate C=O group accepts a hydrogen bond from Y306, the Zn^{2+}-bound hydroxamate N– O^- group accepts a hydrogen bond from H142, and the hydroxamate NH group donates a hydrogen bond to H143. Finally, the benzamide capping group makes two

water-mediated hydrogen bonds with D101 and H180. This array of enzyme-inhibitor interactions is identical in both monomers in the asymmetric unit.

While the SAHA hydroxamate metal coordination and hydrogen bond interactions are identical with those observed in the wild-type enzyme complex (PDB 1T69) (Somoza et al., 2004), hydrogen bond interactions of the benzamide capping group differ because the capping group amide is flipped. However, the lower resolution of the wild-type complex and the lack of well-defined electron density for D101 might suggest that the capping group is not definitively modeled in the wild-type HDAC8–SAHA complex (PDB 1T69) (Somoza et al., 2004). When the structure of the I45T HDAC8–SAHA complex reported herein is compared to the structures of the C153F HDAC8–SAHA complex (PDB 4QA0) and the I243N HDAC8–SAHA complex (PDB 4QA2) (Decroos et al., 2014), there are no differences in inhibitor binding.

Since the Cα atom of residue 45 is rather distant from the catalytic Zn^{2+} ion, the I45T mutation is not expected to influence the binding conformation of the inhibitor. Slight structural differences are observed in the vicinity of the I45T substitution in the structure of the I45T HDAC8–SAHA complex. Moreover, there are slight differences between the two monomers in the asymmetric unit. In monomer A, T45 exists in two alternative conformations (Figure 3A). In one conformation, the hydroxyl group of T45 forms hydrogen bonds with the backbone carbonyl of V41 as well as T316. In the alternative conformation, the hydroxyl group of T45 forms a hydrogen bond with the backbone carbonyl of H42 in addition to H51. Notably, the side chain of H51 adopts two alternative conformations and only forms a hydrogen bond with T45 when oriented inward. In monomer B, H51 only adopts an outward conformation and does not hydrogen bond with T45. All other interactions remain consistent between monomers (Figure 3B). In the wild-type enzyme, the nonpolar I45 residue is incapable of forming hydrogen bonds, so the introduction of the polar T45 side chain leads to the formation of new hydrogen bond interactions. Superposition of I45T HDAC8 with the wild-type enzyme shows that no other major conformational changes are triggered by the I45T substitution (Figure 3C).

2.3. Structure of the E66D/Y306F HDAC8–Ac-RHK$_{Ac}$K$_{Ac}$-AMC complex

The E66D HDAC8 mutant was identified in a girl with autism spectrum, mixed expressive language disorder, normal stature, telecanthus, and other facial features consistent with the HDAC8 clinical phenotype. The Cα atom of E66 is 25 Å away from the active site Zn^{2+} ion.

The E66D/Y306F HDAC8–Ac-RHK$_{Ac}$K$_{Ac}$-AMC complex crystallizes in orthorhombic space group $P2_12_12_1$ and contains two monomers in the asymmetric unit; crystals diffract to 1.84 Å resolution. There are no major conformational differences between the structures of the E66D/Y306F HDAC8–Ac-RHK$_{Ac}$K$_{Ac}$-AMC complex and the previously reported Y306F HDAC8–Ac-RHK$_{Ac}$K$_{Ac}$-AMC complex (PDB 2V5W) (Vannini et al., 2007), and the rmsd is 0.16 Å for 317 Cα atoms. The amide carbonyl group of the scissile acetyllysine residue coordinates to the catalytic Zn^{2+} ion and appears poised for nucleophilic attack by a Zn^{2+}-bound water molecule (Figure 4). Because the activation of the scissile carbonyl requires both coordination to Zn^{2+} and hydrogen bonding to Y306, nucleophilic attack cannot occur in the Y306F mutant due to insufficient polarization of the carbonyl group.

This allows for the crystallographic isolation of an unreacted substrate bound in the enzyme active site. There is no change in the binding conformation of the substrate to Y306F HDAC8 and E66D/Y306F HDAC8, consistent with the relatively invariant K_M values measured for wild-type and E66D HDAC8 enzymes (Table 1).

Subtle structural differences are observed in the vicinity of the E66D substitution (Figure 5). In monomer A, the backbone carbonyl of D66 accepts a hydrogen bond from T69 while the backbone NH group accepts a hydrogen bond from S63 in both the wild-type and mutant enzymes. Additionally, a water-mediated hydrogen bond is formed with nearby residue R164. Electron density interpreted as glycerol is observed near D66, and one of the glycerol hydroxyl groups donates a hydrogen bond to the carboxylate group of D66. In monomer B, this electron density is also interpreted as glycerol. Notably, adjacent residue E65 undergoes a conformational change to an outward orientation in both monomers. Even so, E65 adopts an outward conformation in several other HDAC8 structures, such as D176A/Y306F HDAC8 (PDB 5DC7), H142A/Y306F HDAC8 (PDB 5DC8), and H334R/Y306F HDAC8 (PDB 4QA7) (Decroos et al., 2014; Gantt et al., 2016).

Interestingly, the structure of another CdLS-related mutant, G117E HDAC8 (PDB 5D1B), reveals that the E117 side chain can form a hydrogen bond with E66 (Decroos et al., 2015). The G117E substitution is located in helix B4, ~21 Å away from the catalytic Zn^{2+} ion, and this mutant exhibits 5% residual activity relative to the wild-type enzyme. Conformational changes resulting from the G117E mutation are evident in the nearby loop connecting β-strand 2 to helix B1, which contains E66, and these conformational changes appear to be transmitted through to the L1 loop so as to slightly constrict the active site.

It is interesting that mutations in the E66-G117 region of HDAC8 appear to be consistently associated with CdLS. Both the E66D and G117E mutants are characterized by subtle structural changes in the loop containing E66 that can propagate through the protein scaffolding to the L1 loop flanking the active site cleft. However, there is no clear link between these structural changes and the 10–20-fold loss of catalytic activity in either mutant.

2.4. Structure of the G320R HDAC8–M344 complex

The G320R HDAC8 mutant was first reported in a child diagnosed with CdLS by Deardorff and colleagues (Deardorff et al., 2012) and subsequently observed in an additional child (Parenti et al., 2016). The Cα atom of G320 is 22 Å away from the active site Zn^{2+} ion.

The G320R HDAC8–M344 complex crystallizes in monoclinic space group $P2_1$ and contains two monomers in the asymmetric unit; crystals diffract to 2.4 Å resolution. There are no major conformational differences between this complex and the corresponding complex with the wild-type enzyme (the rmsd for 301 Cα atoms is 0.35 Å). As observed for the binding of SAHA to I45T HDAC8, the hydroxamate group of M344 coordinates to the catalytic Zn^{2+} ion with bidentate geometry and makes a similar array of hydrogen bond interactions with active site residues (Figure 6). No major conformational differences are observed between monomer A and monomer B in the asymmetric unit, but local structural differences are observed near the G320R mutation.

In both monomers, the side chain of R320 is oriented towards solution and donates two poorly-oriented hydrogen bonds to the backbone carbonyl of K325 (Figure 7). These hydrogen bonds cause the loop containing K325 to shift by approximately 1 Å. Additionally, R320 forms hydrogen bonds with two water molecules in monomer A, but these water molecules are not observed in monomer B.

2.5. Structural model of D176G HDAC8

The D176G mutation in HDAC8 was identified as a *de novo* variant in a girl unsuspected of having CdLS prior to exome sequencing (Yuan et al., 2019). We were unable to express D176G HDAC8 for structural study, so we used computational methods to construct a protein model (Figure 8). The energy-minimized model of D176G HDAC8 reveals no major conformational changes in comparison with the experimentally determined structure of D176A/Y306F HDAC8 (the rmsd for 352 Cα atoms is 0.34 Å). Of note, D176 coordinates to one of the monovalent cations (K^+) in the HDAC8 active site; deletion of the carboxylate side chain of this residue leads to K^+ dissociation (Gantt et al., 2016). Additionally, D176 accepts a hydrogen bond from one of the catalytic histidine residues, H142, and stabilizes the positively charged imidazolium cation. The H142 imidazolium group is thought to be an obligatory electrostatic catalyst, stabilizing the anionic transition state resulting from nucleophilic attack at the scissile carbonyl group of acetyllysine (Gantt et al., 2010, 2016). The loss of the D176–H142 hydrogen bond in either D176A or D176G HDAC8 would lower the pKa of H142, which would facilitate proton dissociation to yield the neutral imidazole form. Since the neutral imidazole cannot stabilize the anionic transition state as effectively as the imidazolium cation, significant reductions in k_{cat} and k_{cat}/K_M result (Table 1).

3. Discussion

In general, disease-linked mutations are randomly distributed throughout the HDAC8 protein structure in positions that otherwise might be unlikely targets for *in vitro* mutagenesis (Deardorff et al., 2016). Thus, in addition to providing insight regarding the molecular basis of a congenital birth defect, the study of HDAC8 mutants identified in children diagnosed with CdLS spectrum disorders provides a unique perspective on long-range effects within the protein scaffold that can influence catalysis.

The I45T and G320R mutations are relatively close to each other (Cα–Cα separation = 9 Å) and are located in a region of the HDAC8 structure that is quite distant from the active site (Figure 1). This region of the HDAC8 structure has been explored only once before in the CdLS mutant H334R HDAC8, which exhibits near-normal catalytic activity (Decroos et al., 2014). Intriguingly, the I45T and G320R substitutions significantly influence catalysis, whereas the H334R substitution does not (Table 1). This difference is likely due to the fact that H334 is located on a solvent-exposed loop, whereas I45 and G320 are located on α-helices in the protein interior. Moreover, I45 is contained in a helix-loop-helix motif recently identified in NMR and molecular dynamics studies as a regulatory region that inhibits HDAC8 catalysis (Werbeck et al., 2020). Subtle structural changes in the helix-loop-helix motif lead to an inactive state of the enzyme, which is consistent with our enzymological measurements as well as the crystal structures of I45T HDAC8 and G320R HDAC8 (Figures

3C and 7B). Steady-state kinetic parameters measured for I45T HDAC8 and G320R HDAC8 reveal more than 20-fold reductions in k_{cat} with only minor variations in K_M (Table 1). The deleterious effects on catalysis resulting from mutations in this regulatory region do not result from disruption of the substrate binding mode, but instead result from transition state destabilization.

E66 is located in a different region of the protein structure and is also located in an α-helix (Figure 1). The E66D substitution causes a conformational change in adjacent solvent-exposed residue E65, and subtle conformational changes are visible in the protein scaffold in the vicinity of D66 (Figure 5B). Steady-state kinetic parameters measured for E66D HDAC8 indicate a 12-fold reduction in k_{cat} and a 5-fold increase in K_M, suggesting that both transition state stabilization and substrate binding are moderately compromised in this mutant (Table 1). Even so, the X-ray crystal structure of the E66D/Y306F HDAC8–substrate complex reveals that the substrate binding mode is nearly identical to that observed in the Y306F HDAC8–substrate complex (Figure 4B).

Of the CdLS HDAC8 mutants presented here, D176 is closest to the active site and forms a hydrogen bond with H142. This hydrogen bond stabilizes the positively charged imidazolium form of H142, which serves a key role as an electrostatic catalyst (Gantt et al., 2010, 2016). While we were unable to express D176G HDAC8, structure-function relationships determined for D176A HDAC8 (Gantt et al., 2016) are likely similar to what would be expected for D176G HDAC8. First, deletion of the negatively charged carboxylate side chain of D176 results in the dissociation of the K^+ ion to which it is coordinated. Additionally, the side chain of H142 rotates and shifts 1.4 Å to form a hydrogen bond with Y174. The consequences for catalysis are severe, in that D176A HDAC8 exhibits a 5400-fold reduction in k_{cat} (Table 1). Therefore, even if D176G HDAC8 were capable of being expressed and adopting a stable fold, as represented by our computationally derived model of D176G HDAC8 (Figure 8), structural changes resulting from the loss of the carboxylate side chain would significantly compromise catalysis.

Two K^+ ions normally bind to HDAC8 (Figure 1B), and enzymological studies reveal that these K^+ ions modulate catalytic activity (Gantt et al., 2010). Specifically, the binding of K^+ to the more distant site 21 Å away from the catalytic Zn^{2+} ion activates catalysis – the enzyme is inactive in the absence of K^+. This result indicates that K^+ binding is necessary to stabilize the protein scaffolding in a catalytically competent conformation. In contrast, K^+ binding to the D176 site is inhibitory, decreasing catalytic activity by 11-fold. It is the inhibitory K^+ ion that is lost in D176A HDAC8 and presumably D176G HDAC8 as well. Regardless, catalytic activity is significantly diminished in D176A HDAC8, so other structural changes resulting from the D176A substitution, such as the newly formed hydrogen bond between catalytic residue H142 and Y174 (Gantt et al., 2016), are likely responsible for compromised catalysis.

Genotype-phenotype relationships for HDAC8 are influenced by several factors, including catalytic activity, thermostability, and X-inactivation, so the influence of structure-function relationships for HDAC8 mutations on clinical phenotypes must be interpreted with caution. The structure-function relationships reported here, as well as those previously reported for

other CdLS HDAC8 mutations (Decroos et al., 2014, 2015), indicate that the clinical phenotype of CdLS spectrum disorders can be associated with mutations that have only a modest effect on catalytic activity, although such mutations are often associated with reduced thermostability (Decroos et al., 2014, 2015). Since HDAC8 is encoded by an X-linked gene, differential expression of mutant and wild-type alleles in female patients can result in milder clinical presentations, whereas males bearing the single mutant allele are usually more seriously affected (Kaiser et al., 2014). Even so, a direct correlation of HDAC8 mutant catalytic activity with disease severity is not uniformly established. For example, consider P91L HDAC8, which exhibits 86% residual catalytic activity compared with wild-type HDAC8 (Decroos et al., 2015). The male patient diagnosed with this mutation exhibits major upper limb abnormalities yet only mild intellectual deficits (Kaiser et al., 2014). In contrast, however, two males independently diagnosed with G320R HDAC8, which exhibits a 50-fold reduction in catalytic efficiency k_{cat}/K_M (Table 1), each present with a moderate disease phenotype (Deardorff et al., 2012; Parenti et al., 2016). Accordingly, it is likely that the total cellular concentration of properly folded HDAC8 as well as its catalytic activity influence the severity of CdLS spectrum disorders.

In conclusion, the study of structure-function relationships in HDAC8 mutants identified in children diagnosed with CdLS spectrum disorders illuminates protein structural features both near and distant from the active site that might otherwise go unnoticed. While it is straightforward to establish the functional importance of a residue such as D176 that forms a hydrogen bond with a catalytically obligatory residues such as H142, it is not so straightforward to predict the functional influence of distant residues such as I45 or G320, each of which is 22 Å away from the active site Zn^{2+} ion. The recent identification of this distant region as a regulatory element in the HDAC8 structure reinforces the newly discovered functional importance of these residues and their influence on catalysis (Werbeck et al., 2020). In view of the 62-fold reduction in catalytic efficiency measured for E66D HDAC8 (Table 1), the short α-helix containing this residue may be another such region that could serve a regulatory role in catalysis *in vivo*, e.g., by interacting with regulatory proteins. Future studies will continue to probe the intriguing structure-function relationships of CdLS HDAC8 mutants.

4. Materials and Methods

4.1. General

All reagents, including the inhibitors suberoylanilide hydroxamic acid (SAHA) and M344, were purchased from Sigma-Aldrich. The *Fluor de Lys* HDAC8 assay substrate $RHK_{ac}K_{ac}$-AMC (K_{ac} = acetyllysine, AMC = aminomethylcoumarin) was purchased from Enzo Life Sciences.

4.2. Expression and purification of HDAC8 mutants

CdLS HDAC8 mutants I45T, D176G, and G320R were introduced into the HDAC8-6His-pET20b construct previously described (Dowling et al., 2008) using standard protocols as outlined in the Quickchange site-directed mutagenesis kit (Agilent). The same method was

used to introduce the E66D mutation into the Y306F HDAC8–6His-pET20b construct. Successful introduction of the mutations was confirmed by DNA sequencing.

Except for D176G HDAC8, which we were unable to express, recombinant HDAC8 mutants were expressed in BL21 (DE3) Gold *Escherichia coli* cells and purified according to previously published procedures with minor modifications (Dowling et al., 2008; Decroos et al., 2014). Briefly, 50 mL cultures were grown overnight in Lysogeny Broth (LB) media supplemented with 100 μg/mL ampicillin at 37° C. These growths were used to inoculate six 1 L cultures in minimal media supplemented with 100 μg/mL ampicillin. Cells were grown at 37° C until the OD_{600} reached 0.5, after which the temperature was lowered to 18° C for 30 min. Cultures were then induced by the addition of isopropyl-β-D-thiogalactopyranoside (IPTG, final concentration 0.4 mM) and $ZnCl_2$ (final concentration 100 μM), and grown overnight at 18° C. Cells were harvested and pelleted by centrifugation, then stored at −80° C until purification.

Upon thawing, cells were resuspended in 90 mL of lysis buffer [50 mM Tris (pH 8.0), 500 mM KCl, 5% w/v glycerol, 3 mM β-mercaptoethanol (BME)], supplemented with 115 μM phenylmethanesulfonyl fluoride (PMSF), and lysed on ice by sonication. Cell debris was pelleted by centrifugation, and the supernatant was loaded onto a TALON affinity column (Clontech labs) preequilibrated with lysis buffer. The column was then washed with the lysis buffer supplemented with 10 mM imidazole, and protein was eluted with lysis buffer supplemented with 200 mM imidazole. Protein fractions were pooled, concentrated to approximately 10 mL, and further purified by size exclusion chromatography using a HiLoad 26/60 Superdex column (GE Healthcare Life Sciences) in size exclusion buffer [50 mM Tris (pH 8.0), 150 mM KCl, 5% w/v glycerol, 1 mM tris(2-carboxyethyl)phosphine (TCEP)]. Purified protein was concentrated to approximately 10 mg/mL; concentrations were determined from the absorbance at 280 nm using the calculated extinction coefficient ε = 50,240 $M^{-1}cm^{-1}$ for the single-site mutants and ε = 48,960 $M^{-1}cm^{-1}$ for the double-site mutants.

4.3. Enzyme kinetics

Steady-state kinetics were measured using the previously described Fluor-de-Lys assay (Dowling et al., 2008; Decroos et al., 2014, 2015). In this assay, the tetrapeptide substrate $RHK_{ac}K_{ac}$-AMC is deacetylated by HDAC8. After quenching the reaction at fixed timepoints, the K ac-AMC amide bond is cleaved using a protease developer solution to result in a measurable fluorescence shift (excitation wavelength = 360 nm, emission wavelength = 460 nm).

HDAC8 (final concentration = 0.5 μM for wild-type enzyme and I45T, E66D, D176G, and G320R mutants) was incubated with substrate (final concentration ranged from 0–2 mM) in assay buffer [25 mM Tris (pH 8.2), 137 mM NaCl, 2.7 mM KCl, 1 mM $MgCl_2$] for 5 min (final volume = 50 μL). The reaction was quenched with 50 μL of Developer II solution containing 200 μM of inhibitor M344. After 45 min, the 100 μL mixture was transferred to a 96-well plate and fluorescence was measured using a Tecan Infinite M1000Pro plate reader.

To calculate HDAC8 activity, measurements were converted into product formation using the Fluor-de-Lys standard curve according to the kit protocol. Data were analyzed using GraphPad Prism version 5.00 for MAC OS X (GraphPad software, La Jolla CA, www.graphpad.com). Assays were performed in triplicate at 24.3 °C. Non-linear regression fits to the Michaelis-Menten equation were used to determine steady-state parameters.

4.4. Crystallization

For cocrystallization of the I45T HDAC8–SAHA complex, a 0.6 μL drop of protein solution [5.0 mg/mL I45T HDAC8, 50 mM Tris (pH 8.0), 150 mM KCl, 30 mM glycylglycylglycine, 5% glycerol (v/v), 1 mM TCEP, 2 mM SAHA, and 5% v/v dimethylsulfoxide (DMSO)] was added to a 0.6 μL drop of precipitant solution [0.1 M imidazole (pH 7.0), 15% polyethylene glycol (PEG) 35,000, and 4 mM TCEP] and equilibrated against a 100 μL reservoir of precipitant solution at 21°C. Crystals formed within 1–2 days and were soaked in a cryoprotectant solution consisting of mother liquor supplemented with 25% ethylene glycol prior to flash-cooling in liquid nitrogen.

For cocrystallization of the E66D/Y306F HDAC8–RHK$_{Ac}$K$_{Ac}$-AMC complex, a 0.7 μL drop of protein solution [5.0 mg/mL E66D/Y306F HDAC8, 50 mM Tris (pH 8.0), 150 mM KCl, 30 mM glycylglycylglycine, 5% glycerol (v/v), 1 mM TCEP, and 2 mM RHK$_{Ac}$K$_{Ac}$-AMC] was added to a 0.7 μL drop of precipitant solution [0.1 M Tris (pH 8.0), 20% PEG 6,000, and 4 mM TCEP] and equilibrated against a 100 μL reservoir of precipitant solution at 21°C. Crystals formed within 1–2 days and were soaked in a cryoprotectant solution consisting of mother liquor supplemented with 25% ethylene glycol prior to flash-cooling in liquid nitrogen.

For cocrystallization of the G320R HDAC8–M344 complex, a 0.5 μL drop of protein solution [4.0 mg/mL G320R HDAC8, 50 mM Tris (pH 8.0), 150 mM KCl, 30 mM glycylglycylglycine, 5% glycerol (v/v), 1 mM TCEP, 2 mM M344, and 5% v/v DMSO] was added to a 0.5 μL drop of precipitant solution [0.1 M MES (pH 5.3), 3% PEG 1,500, and 4 mM TCEP] and equilibrated against a 100 μL reservoir of precipitant solution at 21°C. Crystals formed within 1–2 days and were soaked in a cryoprotectant solution consisting of mother liquor supplemented with 25% ethylene glycol prior to flash-cooling in liquid nitrogen.

4.5. Data collection, structure determination, and refinement

X-ray diffraction data were collected from crystals on Northeastern Collaborative Access Team beamline 24-ID-E at the Advanced Photon Source, Argonne National Laboratory, for the I45T HDAC8–SAHA and E66D/Y306F HDAC8–RHK$_{Ac}$K$_{Ac}$-AMC complexes. These data were indexed, integrated, and scaled using HKL2000 (Otwinowski and Minor, 1997). X-ray diffraction data for the G320R HDAC8–M344 complex were collected on beamline 14–1 at the Stanford Synchrotron Radiation Lightsource. These data were indexed and integrated using iMosflm (Battye et al., 2011) and scaled using Aimless (Evans et al., 2013) in the CCP4 program suite (Winn et al., 2011).

For each crystal structure determination, the initial electron density map was phased by molecular replacement using PHASER (McCoy et al., 2007) and the structure of H143A

HDAC8 (PDB 3EWF) less ligand and solvent molecules as a search probe. Model building and refinement were performed with COOT and PHENIX, respectively (Emsley et al., 2010, Adams et al., 2010). Solvent molecules and ligands were modeled during the final stages of refinement. Structure validation was performed using MOLPROBITY (Chen et al., 2010). All data collection and refinement statistics are recorded in Table 2.

4.5. Molecular modeling of D176G HDAC8

The MD simulation was run using GROMACS (GROningen MAchine for Chemical Simulation). The starting point for the MD simulation was the crystal structure of wild-type HDAC8 in complex with largazole (PDB accession code 3RQD). The coordinate file was stripped of all water and inhibitor atoms and the amino acid substitution D176G was made using PyMol. The K^+ ion coordinated by D176 was removed. The second K^+ ion and the catalytic Zn^{2+} ion were retained in the coordinate file, consistent with the deletion of the D176 side chain in D176A HDAC8. The pdb2gmx command was used to generate a Gromacs-compatible topology, position restraint and structure file using the AMBER99SB-ILDN force field. A cubic box was defined with the faces 12 Å from the protein surface. The box was filled with water molecules and Na^+ and Cl^- ions added to a concentration of 0.1 M to neutralize the system. The protein-solvent system was subject to energy minimization using the steepest descent method.

5. PDB accession numbers

Atomic coordinates and structure factor amplitudes of the I45T HDAC8–SAHA complex, the E66D/Y306F HDAC8–RHK$_{Ac}$K$_{Ac}$-AMC complex, and the G320R HDAC8–M344 complex have been deposited in the Protein Data Bank (www.rcsb.org) with accession numbers 7JVU, 7JVV, and 7JVW, respectively.

Acknowledgements

We thank the U.S. National Institutes of Health (NIH) for grant GM49758 in support of this research. This research is based upon research conducted at the Northeastern Collaborative Access Team beamlines, which are funded by the National Institute of General Medical Sciences of the NIH (P30 GM124165). The Eiger 16M detector on the 24-ID-E beam line is funded by an NIH-ORIP HEI grant (S10OD021527). This research utilized resources of the Advanced Photon Source, a U.S. Department of Energy (DOE) Office of Science User Facility operated for the DOE Office of Science by Argonne National Laboratory under Contract No. DEAC02-06CH11357. Additionally, this research utilized the Stanford Synchrotron Radiation Lightsource (SSRL), SLAC National Accelerator Laboratory, which is supported by the DOE Office of Science, Office of Basic Energy Sciences, under Contract No. DE-AC02-76SF00515. The SSRL Structural Molecular Biology Program is supported by the DOE Office of Biological and Environmental Research, and by the National Institute of General Medical Sciences of the NIH (P41GM103393).

References

Adams PD, Afonine PV, Bunkoczi G, Chen VB, Davis IW, Echols N, Headd JJ, Hung L, Kapral GJ, Grosse-Kunstleve RW, McCoy AJ, Moriarty NW, Oeffner R, Read RJ,Richardson DC, Richardson JS, Terwilliger TC, and Zwart PH (2010) PHENIX: a comprehensive python-based system for macromolecular structure solution Acta Cryst. D66, 213–221.

Battye TGG, Kontogiannis L, Johnson O, Powell HR, Leslie AGW, 2011. iMOSFLM: A new graphical interface for diffraction-image processing with MOSFLM. Acta Cryst. D67, 271–281.

Brachmann W (1916) Ein Fall von symmetrischer Monodaktylie durch Ulnadefekt, mit symmetrischer Flughautbildung in den Ellenbeugen, sowie anderen Abnormitäten (Zwerghaftigkeit, Halsrippen, Behaarung). Jahrbuch für Kinderheilkunde und physische Erziehung 84, 225–235.

Chen VB, Arendall WB III, Headd JJ, Keedy DA, Immormino RM, Kapral GJ, Murray LW, Richardson JS, Richardson DC, 2010. MolProbity: all-atom structure validation for macromolecular crystallography. Acta Cryst. D66, 12–21.

Deardorff MA, Bando M, Nakato R, Watrin E, Itoh T, Minamino M, Saitoh K, Komata M, Katou Y, Clark D, Cole KE, De Baere E, Decroos C, Di Donato N, Ernst S, Francey LJ, Gyftodimou Y, Hirashima K, Hullings M, Ishikawa Y, Jaulin C, Kaur M, Kiyono T, Lombardi PM, Magnaghi-Jaulin L, Mortier GR, Nozaki N, Petersen MB, Seimiya H, Siu VM, Suzuki Y, Takagaki K, Wilde JJ, Willems PJ, Prigent C, Gillessen-Kaesbach G, Christianson DW, Kaiser FJ, Jackson LG, Hirota T, Krantz ID, and Shirahige K (2012) HDAC8 mutations in Cornelia de Lange syndrome affect the cohesin acetylation cycle. Nature 489, 313–317. [PubMed: 22885700]

Deardorff MA, Porter NJ, Christianson DW (2016) Structural aspects of HDAC8 mechanism and dysfunction in Cornelia de Lange Syndrome spectrum disorders. Protein Sci. 25, 1965–1976. [PubMed: 27576763]

Deardorff MA, Noon SE, Krantz ID (2020) Cornelia de Lange Syndrome. GeneReviews, Adam MP, Ardinger HH, Pagon RA, Eds. Seattle (WA): University of Washington, 1993–2020.

Decroos C, Bowman CM, Moser J-AS, Christianson KE, Deardorff MA, Christianson DW (2014) Compromised structure and function of HDAC8 mutants identified in Cornelia de Lange Syndrome spectrum disorders. ACS Chem. Biol 9, 2157–2164. [PubMed: 25075551]

Decroos C, Christianson NH, Gullett LE, Bowman CM, Christianson KE, Deardorff MA, Christianson DW (2015) Biochemical and structural characterization of HDAC8 mutants associated with Cornelia de Lange Syndrome spectrum disorders. Biochemistry 54, 6501–6513. [PubMed: 26463496]

De Lange C (1933) Sur un type nouveau de dégénération (typus Amstelodamensis) Arch. Méd. Enfants 36, 713–719.

De Lange C (1938) Nouvelle observation du “typus Amstelodamensis” et examen anatomo-pathologique de ce type. Arch. Méd. Enfants 41, 193–203.

Dowling DP, Gantt SL, Gattis SG, Fierke CA, Christianson DW, 2008. Structural studies of human histone deacetylase 8 and its site-specific variants complexed with substrate and inhibitors. Biochemistry 47, 13554–13563. [PubMed: 19053282]

Dowsett L, et al. (2018) Cornelia de Lange syndrome in diverse populations. Am. J. Med. Genet 179A, 150–158.

Emsley P, Lohkamp B, Scott WG, Cowtan K, 2010. Features and development of Coot. Acta Cryst D66, 486–501.

Evans PR, Murshudov GN, 2013. How good are my data and what is the resolution? Acta Cryst D69, 1204–1214.

Feng L, Zhou D, Zhang Z, Liu Y, and Yang Y (2014) Exome sequencing identifies a *de novo* mutation in HDAC8 associated with Cornelia de Lange syndrome. J. Hum. Genet 59, 536–539. [PubMed: 25102094]

Gantt SL, Gattis SL, and Fierke CA (2006) Catalytic activity and inhibition of human histone deacetylase 8 is dependent on the identity of the active site metal ion. Biochemistry 45, 6170–6178. [PubMed: 16681389]

Gantt SL, Joseph CG, and Fierke CA (2010) Activation and inhibition of histone deacetylase 8 by monovalent cations. J. Biol. Chem 285, 6036–6043. [PubMed: 20029090]

Gantt SM, Decroos C, Lee MS, Gullett LE, Bowman CM, Christianson DW Fierke CA (2016) General base-general acid catalysis in human histone deacetylase 8. Biochemistry 55, 820–832. [PubMed: 26806311]

Gruber S, Haering CH, Nasmyth K (2003) Chromosomal cohesin forms a ring. Cell 112, 765–777. [PubMed: 12654244]

Gurovich Y, Hanani Y, Bar O, Nadav G, Fleischer N, Gelbman D, Basel-Salmon L, Krawitz PM, Kamphausen SB, Zenker M, Bird LM, Gripp KW (2019) Identifying facial phenotypes of genetic disorders using deep learning. Nat. Medicine 25, 60–64.

Hons MT, Hus in't Veld PJ, Kaesler J, Rombaut P, Schleiffer A, Herzog F, Stark H, Peters J-M (2016) Topology and structure of an engineered human cohesin complex bound to Pds5B. Nat. Commun 7, 12523. [PubMed: 27549742]

Izumi K (2016) Disorders of transcriptional regulation: an emerging category of multiple malformation syndromes. Mol. Syndromol 7, 262–273. [PubMed: 27867341]

Kaiser FJ, Ansari M, Braunholz D, Gil-Rodríguez MC, Decroos C, Wilde JJ, Fincher CT, Kaur M, Bando M, Amor DJ, Atwal PS, Bahlo M, Bowman CM, Bradley JJ, Brunner HG, Clark D, Del Campo M, Di Donato N, Diakumis P, Dubbs H, Dyment DA, Eckhold J, Ernst S, Ferreira JC, Francey LJ, Gehlken U, Guillén-Navarro E, Gyftodimou Y, Hall BD, Hennekam R, Hudgins L, Hullings M, Hunter JM, Yntema H, Innes AM, Kline AD, Krumina Z, Lee H, Leppig K, Lynch SA, Mallozzi MB, Mannini L, McKee S, Mehta SG, Micule I, Care4Rare Canada Consortium, Mohammed S, Moran E, Mortier GR, Moser J-AS, Noon SE, Nozaki N, Nunes L, Pappas JG, Penney LS, Pérez-Aytés A, Petersen MB, Puisac B, Revencu N, Roeder E, Saitta S, Scheuerle AE, Schindeler KL, Siu VM, Stark Z, Strom SP, Thiese H, Vater I, Willems P, Williamson K, Wilson LC, University of Washington Center for Mendelian Genomics, Hakonarson H, Quintero-Rivera F, Wierzba J, Musio A, Gillessen-Kaesbach G, Ramos FJ, Jackson LG, Shirahige K, Pié J, Christianson DW, Krantz ID, Fitzpatrick DR, and Deardorff MA (2014) Loss of function HDAC8 mutations cause a phenotypic spectrum of Cornelia de Lange Syndrome-like features, ocular hypertelorism, large fontanelle and X-linked inheritance. Hum. Mol. Genet 23, 2888–2900. [PubMed: 24403048]

Kline AD, Moss JF, Selicorni A, Bisgaard A-M, Deardorff MA, Gillett PM, Ishman SL, Kerr LM, Levin AV, Mulder PA, Ramos FJ, Wierzba J, Ajmone PF, Axtell D, Blagowidow N, Cereda A, Costantino A, Cormier-Daire V, FitzPatrick D, Grados M, Groves L, Guthrie W, Huisman S, Kaiser FJ, Koekkoek G, Levis M, Mariani M, McCleery JP, Menke LA, Metrena A, O'Connor J, Oliver C, Pie J, Piening S, Potter CJ, Quaglio AL, Redeker E, Richman D, Rigamonti C, Shi A, Tümer Z, Van Balkom IDC, Hennekam RC (2018) Diagnosis and management of Cornelia de Lange syndrome: first international consensus statement. Nat. Rev. Genet 19, 649–666. [PubMed: 29995837]

Loos HS, Wieczorek D, Würtz RP, von der Malsburg C, Horsthemke B (2003) Computer-based recognition of dysmorphic faces. Eur. J. Hum. Genet 11, 555–560. [PubMed: 12891374]

McCoy AJ, Grosse-Kunstleve RW, Adams PD, Winn MD, Storoni LC, Read RJ, 2007. Phaser crystallographic software. J. Appl. Cryst 40, 658–674. [PubMed: 19461840]

Otwinowski Z, and Minor W (1997) Processing of X-ray diffraction data collected in oscillation mode. Methods Enzymol 276, 307–326.

Parenti I, Gervasini C, Pozojevic J, Wendt KS, Watrin E, Azzollini J, Braunholz D, Buiting K, Cereda A, Engels H, Garavelli L, Glazar R, Graffmann B, Larizza L, Lüdecke HJ, Mariani M, Masciadri M, Pié J, Ramos FJ, Russo S, Selicorni A, Stefanova M, Strom TM, Werner R, Wierzba J, Zampino G, Gillessen-Kaesbach G, Wieczorek D, Kaiser FJ (2016) Expanding the clinical spectrum of the 'HDAC8-phenotype' – implications for molecular diagnostics, counseling and risk prediction. Clin Genet 89, 564–573. [PubMed: 26671848]

Rohatgi S, Clark D, Kline AD, Jackson LG, Pie J, Siu V, Ramos FJ, Krantz ID, Deardorff MA (2010) Facial diagnosis of mild and variant CdLS: insights from a dysmorphologist survey. Am. J. Med. Genet. A 152, 1641–1653.

Sarogni P, Pallotta MM, Musio A (2019) Cornelia de Lange syndrome: from molecular diagnosis to therapeutic approach. J. Med. Genet 0, 1–7. Doi: 10.1136/jmedgenet-2019-106277.

Shi Z, Gao H, Bai X. c., Yu H (2020) Cryo-EM structure of the human cohesin-NIPBL-DNA complex. Science 368, 1454–1459. [PubMed: 32409525]

Somoza JR, Skene RJ, Katz BA, Mol C, Ho JD, Jennings AJ, Luong C, Arvai A, Buggy JJ, Chi E, Tang J, Sang BC, Verner E, Wynands R, Leahy EM, Dougan DR, Snell G, Navre M, Knuth MW, Swanson RV, McRee DE, and Tari LW (2004) Structural snapshots of human HDAC8 provide insights into the class I histone deacetylases. Structure 12, 1325–1334. [PubMed: 15242608]

Vannini A, Volpari C, Gallinari P, Jones P, Mattu M, Carfí A, De Francesco R, Steinkühler C, Di Marco S (2007) Substrate binding to histone deacetylases as shown by the crystal structure of the HDAC8–substrate complex. EMBO Rep 8, 879–884. [PubMed: 17721440]

Werbeck ND, Shukla VK, Kunze MBA, Yalinca H, Pritchard RB, Siemons L, Mondal S, Greenwood SOR, Kirkpatrick J, Marson CM, Hansen DF (2020) A distal regulatory region of a class I human histone deacetylase. Nat. Commun 11, 3841. [PubMed: 32737323]

Winn MD, Ballard CC, Cowtan KD, Dodson EJ, Emsley P, Evans PR, Keegan RM, Krissinel EB, Leslie AGW, McCoy A, McNicholas SJ, Murshudov GN, Pannu NS, Potterton EA, Powell HR, Read RJ, Vagin A, Wilson KS (2011) Overview of the CCP4 suite and current developments. Acta Cryst D67, 235–242.

Yuan B, Neira J, Pehlivan D, Santiago-Sim T, Song X, Rosenfeld J, Posey JE, Patel V, Jin W, Adam MP, Baple EL, Dean J, Fong C-T, Hickey SE, Hudgins L, Leon E, Madan-Khetarpal S, Rawlins L, Rustad CF, Stray-Pedersen A, Tveten K, Wenger O, Diaz J, Jenkens L, Martin L, McGuire M, Pietryga M, Ramsdell L, Slattery L, DDD Study, Abid F, Bertuch A, Grange D, Immken L, Schaaf CP, Van Esch H, Bi W, Cheung SW, Breman AM, Smith JL, Shaw C, Crosby AH, Eng C, Yang Y, Lupski JR, Xiao R, Liu P (2019) Clinical exome sequencing reveals locus heterogeneity and phenotypic variability of cohesinopathies. Genet. Med 21, 663–675. [PubMed: 30158690]

Highlights

- Missense mutations in HDAC8 can cause Cornelia de Lange Syndrome
- HDAC8 mutations I45T, E66D, D176G, and G320R HDAC8 result in loss of function
- Crystallographic and computational approaches yield models of these mutants
- Structural analysis reveals a molecular basis for compromised catalysis

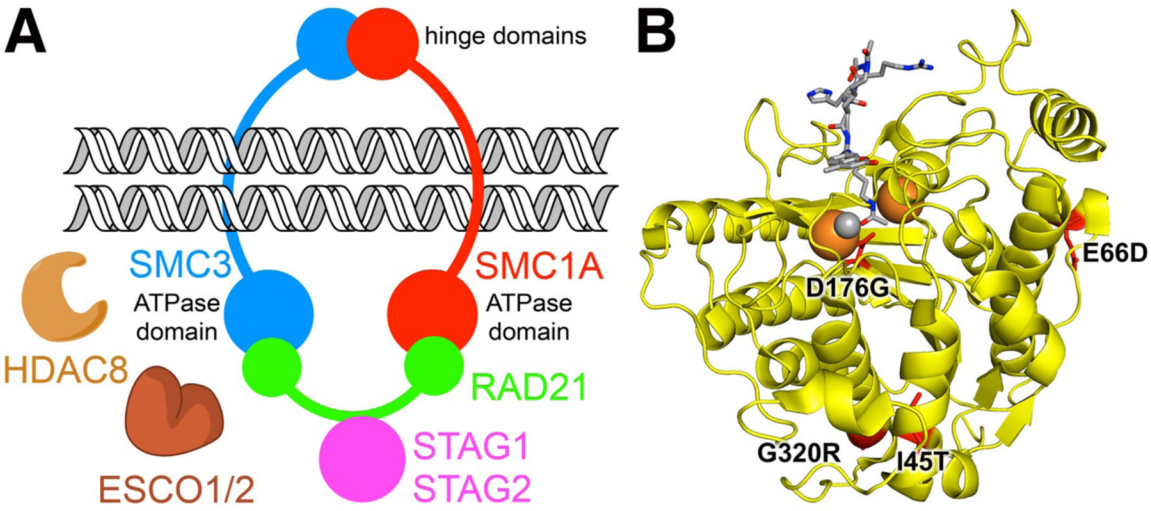

Figure 1.

(A) Cohesin structural proteins SMC1A and SMC3 associate through their hinge domains and encircle sister chromatids during cell division; RAD21 associates with the ATPase domains of SMC1A and SMC3, and STAG1 or STAG2 binds to RAD21 to stabilize cohesin closure. ESCO1 and ESCO2 are responsible for acetylation of K105 and K106 in the ATPase domain of SMC3, and HDAC8 is responsible for SMC3 deacetylation. Reproduced from Deardorff et al., 2016. **(B)** The I45T, E66D, D176G, and G320R mutations in HDAC8 have been identified in children diagnosed with Cornelia de Lange Syndrome (CdLS) spectrum disorders. These residues are mapped onto the structure of Y306F HDAC8 complexed with the assay substrate Ac-RHKAcKAc-AMC (Ac = acetyl, Kac = acetyllysine, AMC = aminomethylcoumarin) (PDB 2V5W). Color code: HDAC8, yellow, CdLS mutations, red; Zn^{2+}, small gray sphere; K^{+} ions, large orange spheres; substrate, stick figure with C = gray, N = blue, O = red.

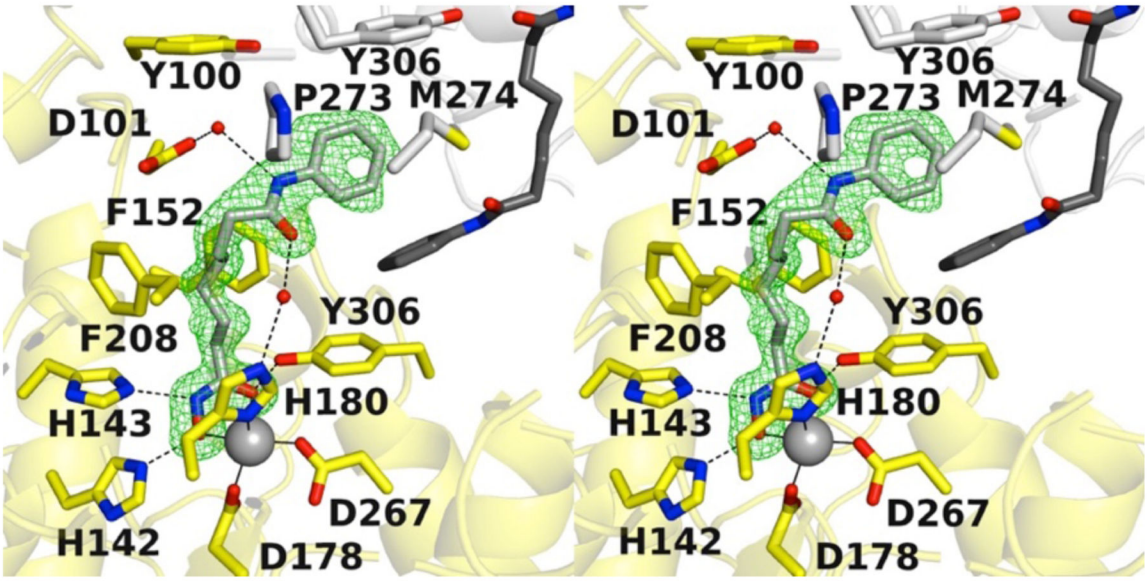

Figure 2.

Polder omit map of SAHA bound in the active site of I45T HDAC8 (PDB 7JVU; monomer A, contoured at 4.0 σ). Atoms are color-coded as follows: C = yellow (monomer A), light gray (monomer B), gray (SAHA, monomer A), or dark gray (SAHA, monomer B), N = blue, O = red, S = light yellow, Zn^{2+} = gray sphere, and solvent = small red spheres. Metal coordination and hydrogen bond interactions are indicated by solid and dashed black lines, respectively.

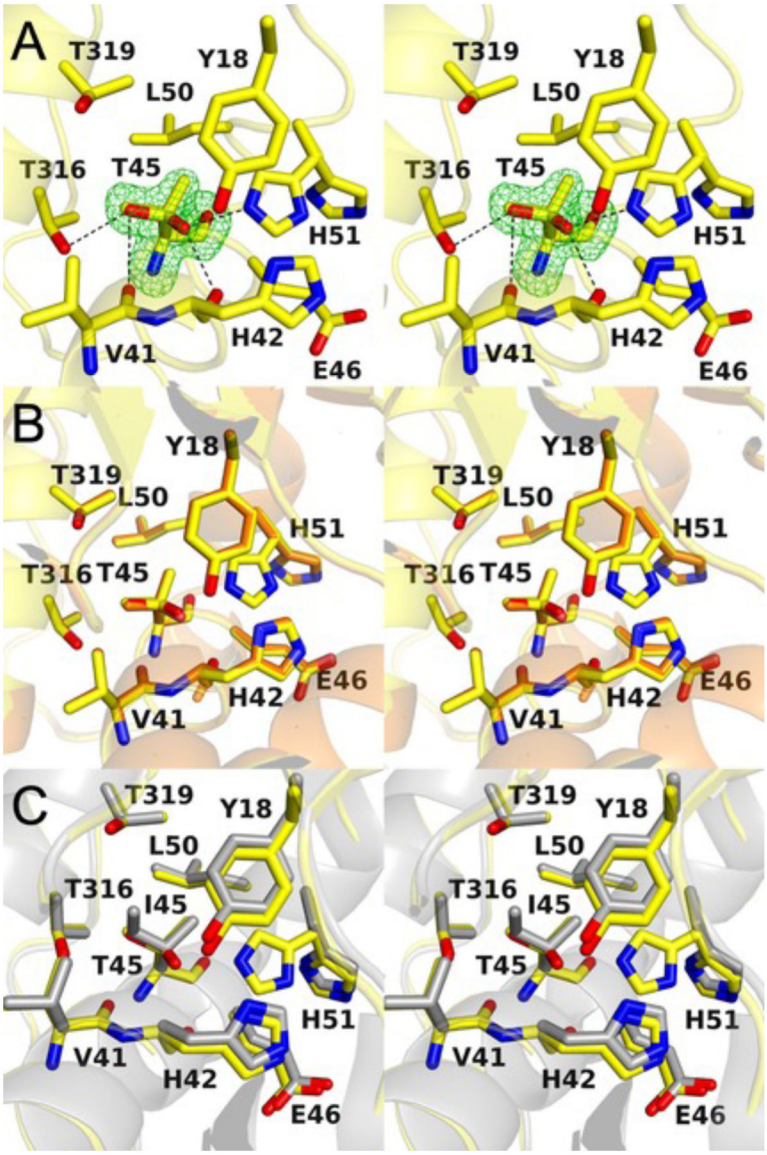

Figure 3.

(A) Polder omit map of T45 in the I45T HDAC8–SAHA complex (PDB 7JVU; monomer A, contoured at 3.5 σ). Atoms are color-coded as follows: C = yellow, N = blue, O = red. Hydrogen bond interactions are indicated by dashed black lines, respectively. **(B)** Superposition of the I45T HDAC8–SAHA complex shown in (A) with monomer B in the same structure (color-coded with C = orange). **(C)** Superposition of the I45T HDAC8–SAHA complex shown in (A) with the wild-type HDAC8–SAHA complex (PDB 1T69). Atoms are color-coded as follows: C = yellow (I45T HDAC8) or gray (wild-type HDAC8), N = blue, O = red.

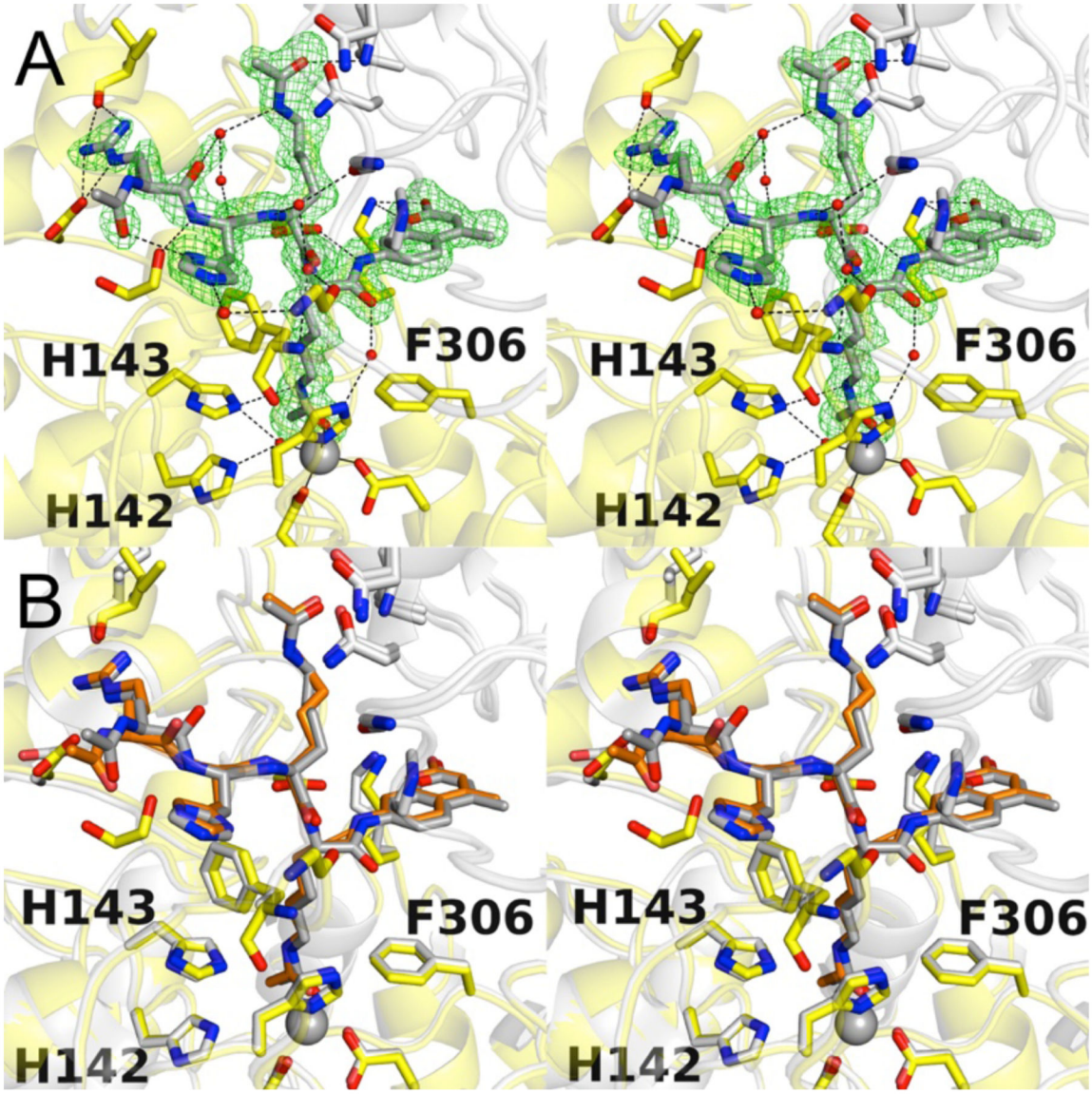

Figure 4.

(A) Polder omit map of the substrate in the E66D/Y306F HDAC8–Ac-RHKAcKAc-AMC complex (PDB 7JVV; monomer A, contoured at 5.0 σ). Atoms are color-coded as follows: C = yellow (monomer A), light gray (monomer B), or gray (substrate), N = blue, O = red, Zn^{2+} = gray sphere, and solvent = small red spheres. Metal coordination and hydrogen bond interactions are indicated by solid and dashed black lines, respectively. **(B)** Superposition of the E66D/Y306F HDAC8–Ac-RHK$_{Ac}$K$_{Ac}$-AMC complex shown in (A) with the structure of the Y306F HDAC8–Ac-RHK$_{Ac}$K$_{Ac}$-AMC complex (PDB 2V5W).

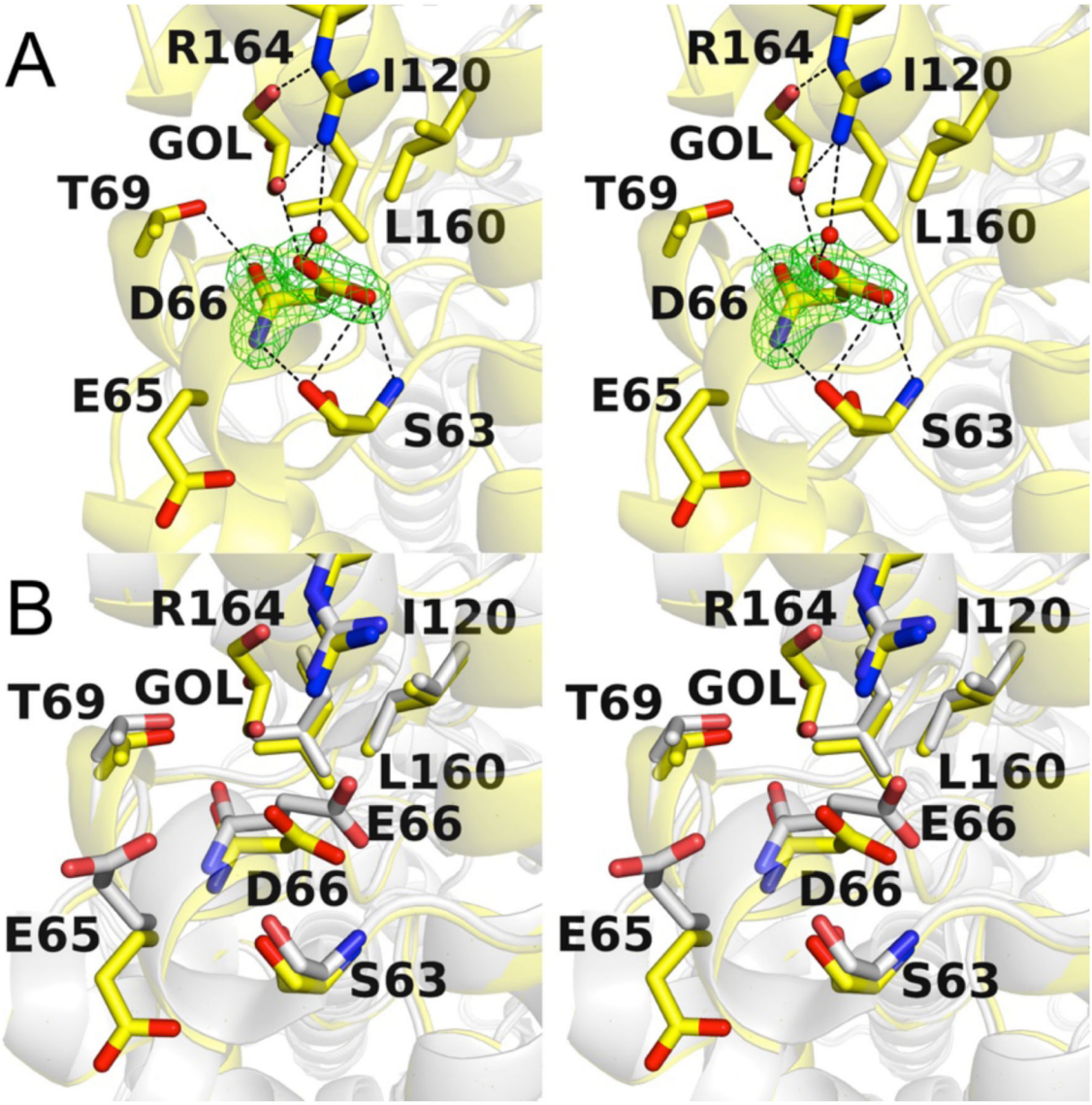

Figure 5.

(A) Polder omit map of D66 in the E66D/Y306F HDAC8–RHKACKAC-AMC complex (PDB 7JVV; monomer A, contoured at 3.0 σ). Atoms are color-coded as follows: C = yellow (monomer A) or light gray (monomer B), N = blue, O = red, and solvent = small red spheres; GOL = glycerol. Hydrogen bond interactions are indicated by dashed black lines. **(B)** Superposition of the E66D/Y306F HDAC8–Ac-RHK$_{Ac}$K$_{Ac}$-AMC complex shown in (A) with the structure of the Y306F HDAC8–Ac-RHK$_{Ac}$K$_{Ac}$-AMC complex (PDB 2V5W). Atoms are color-coded as follows: C = yellow (E66D/Y306F HDAC8) or gray (wild-type HDAC8), N = blue, O = red.

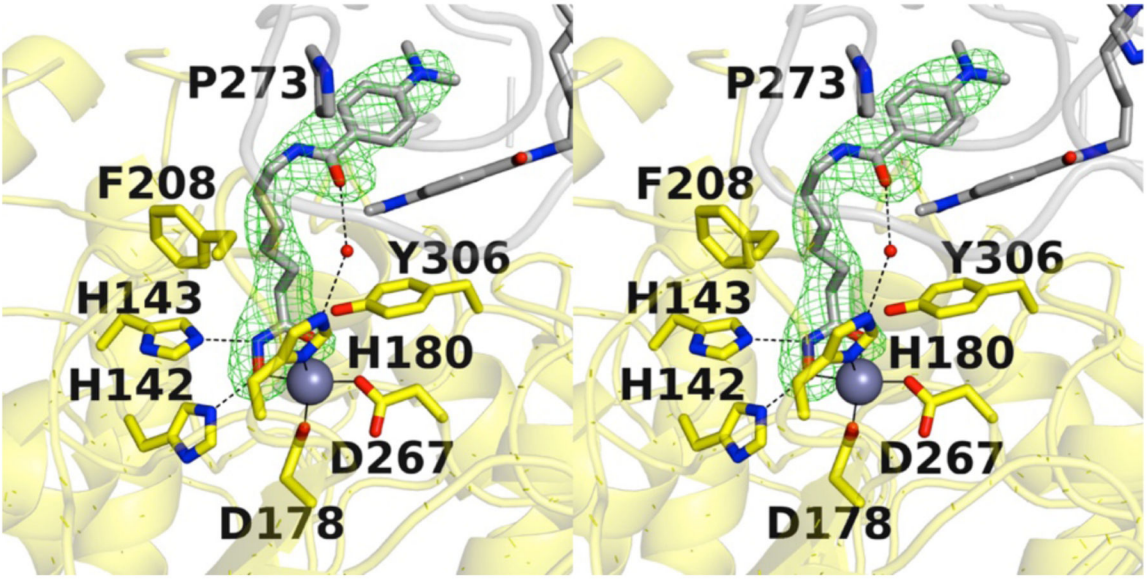

Figure 6.

Polder omit map of the inhibitor M344 in the G320R HDAC8–M344 complex (PDB 7JVW; monomer A, contoured at 3.5 σ). Atoms are color-coded as follows: C = yellow (monomer A), light gray (monomer B), gray (inhibitor), or dark gray (inhibitor bound to monomer B), N = blue, O = red, Zn^{2+} = gray sphere, and solvent = small red spheres. Metal coordination and hydrogen bond interactions are indicated by solid and dashed black lines, respectively.

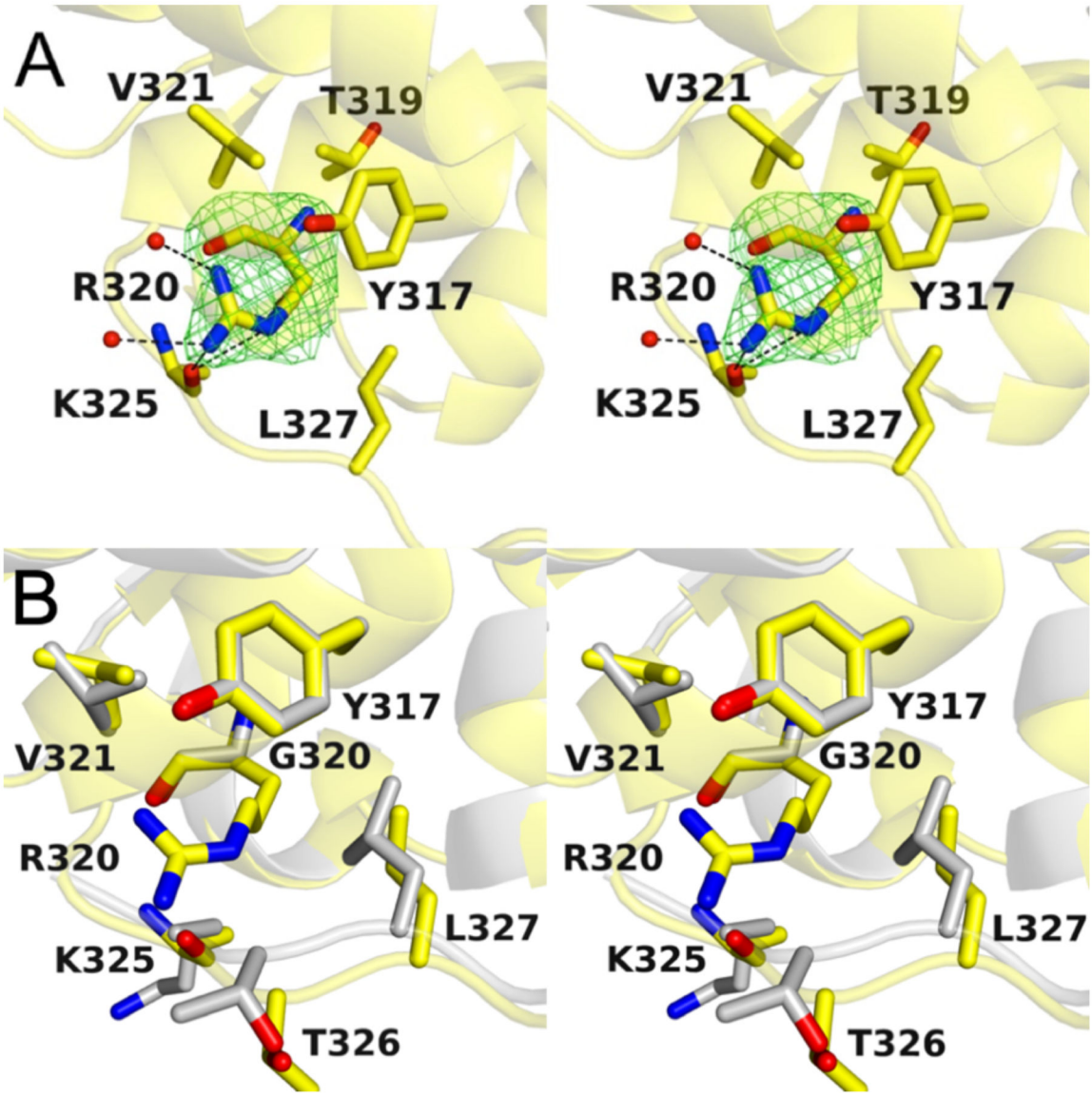

Figure 7.

(A) Polder omit map of R320 in the G320R HDAC8–M344 complex (PDB 7JVW; monomer A, contoured at 3.5 σ). Atoms are color-coded as follows: C = yellow, N = blue, O = red, and solvent = small red spheres. Hydrogen bond interactions are indicated by dashed black lines. **(B)** Superposition of the G320R HDAC8–M344 complex shown in (A) with the wild-type HDAC8–M344 complex (PDB 1T67). Atoms are color-coded as follows: C = yellow (G320R HDAC8) or gray (wild-type HDAC8), N = blue, O = red.

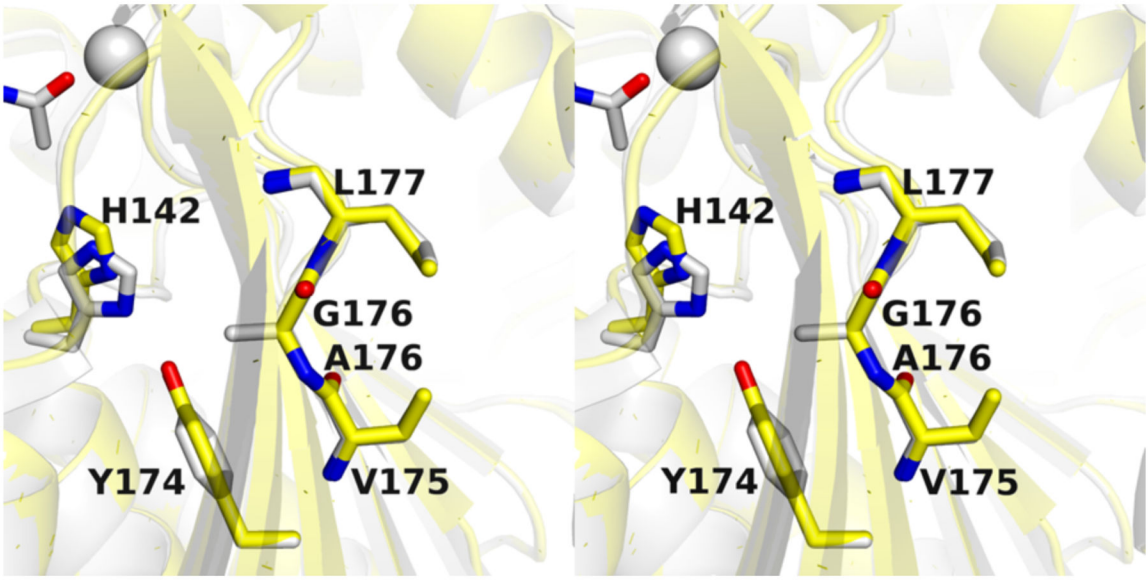

Figure 8.

Superposition of the computationally-derived model of D176G HDAC8 and the experimentally-determined structure of D176A/Y306F HDAC8 complexed with an assay substrate (PDB 5DC7). Atoms are color-coded as follows: C = yellow (D176G HDAC8) or gray (D176A HDAC8), N = blue, O = red, Zn^{2+} = gray sphere.

Table 1.

Steady-State Kinetics of CdLS HDAC8 Mutants

Mutant	k_{cat} (s^{-1})	*K*M (μM)	k_{cat}/K_M ($M^{-1}s^{-1}$)
wild-type	0.59 ± 0.07	300 ± 100	2100
I45T	0.028 ± 0.003	900 ± 200	33
E66D	0.047 ± 0.004	1400 ± 200	34
D176G*	—	—	—
D176A*	0.00011 ± 0.00007	150 ± 20	0.75
G320R	0.026 ± 0.002	600 ± 100	42

*We were unable to express D176G HDAC8, so the previously reported kinetic parameters for D176A HDAC8 are listed as reasonable surrogates (Gantt et al., 2016).

Table 2.

Data Collection and Refinement Statistics for CdLS HDAC8 Mutants

Mutant–Ligand	I45T HDAC8–SAHA	E66D/Y306F HDAC8–RHK$_{Ac}$K$_{Ac}$-AMC	G320R HDAC8–M344
Unit Cell			
Space group	$P2_1$	$P2_12_12_1$	$P2_1$
a, b, c (Å)	53.3, 84.2, 94.3	82.0, 97.5, 104.3	53.0, 82.8, 94.5
α, β, γ (°)	90.0, 99.1, 90.0	90.0, 90.0, 90.0	90.0, 98.8, 90.0
Data Collection			
Resolution (Å)[a]	55.91–1.50 (1.55–1.50)	44.15–1.84 (1.91–1.84)	82.75–2.40 (2.49–2.40)
Total/unique no. of reflections	733,202/130,929	367,452/70,664	115,696/30,670
R_{merge}[a,b]	0.074 (0.795)	0.111 (0.760)	0.148 (0.961)
R_{pim}[a,b]	0.034 (0.389)	0.052 (0.355)	0.090 (0.571)
$CC_{1/2}$[a,d]	0.998 (0.757)	0.999 (0.759)	0.981 (0.578)
I/σ(I)[a]	19.5 (2.3)	13.8 (2.3)	8.7 (1.7)
Redundancy[a]	5.6 (5.1)	5.2 (5.1)	3.8 (3.8)
Completeness (%)[a]	99.8 (99.9)	97.5 (99.4)	97.4 (96.0)
Refinement			
No. of reflections used in refinement/test set	130,893/12,993	70,607/6,933	30,556/2,981
R_{work}[a,e]	0.164 (0.241)	0.165 (0.238)	0.195 (0.283)
R_{free}[a,e]	0.185 (0.272)	0.197 (0.284)	0.254 (0.369)
No. of nonhydrogen atoms:			
protein	5,698	5,667	5,416
ligand	72	74	50
solvent	635	453	145
Average *B*-factors (Å^2)			
protein	22	20	41
ligand	27	23	45
solvent	32	27	37
Root-mean-square deviation from ideal geometry			
bonds (Å)	0.005	0.006	0.008
angles (°)	0.8	0.8	0.9
Ramachandran plot (%)[f]			
favored	98.48	97.92	95.23
allowed	1.52	2.08	4.63
outliers	0.00	0.00	0.14

[a]Values in parentheses refer to data in the highest shell.

[b] $R_{merge} = \sum_{hkl} \sum_i \left| I_{i,hkl} - \langle I \rangle_{hkl} \right| / \sum_{hkl} \sum_i I_{i,hkl}$, where $\langle I \rangle_{hkl}$ is the average intensity calculated for reflection *hkl* from replicate measurements.

[c] $R_{p.i.m.} = \left(\sum_{hkl} (1/(N-1))^{1/2} \sum_i \left| I_{i,hkl} - \langle I \rangle_{hkl} \right| \right) / \sum_{hkl} \sum_i I_{i,hkl}$, where $\langle I \rangle_{hkl}$ is the average intensity calculated for reflection *hkl* from replicate measurements and N is the number of reflections

[d] Pearson correlation coefficient between random half-datasets.

[e] $R_{work} = \sum ||F_o| - |F_c|| / \sum |F_o|$ for reflections contained in the working set. $|F_o|$ and $|F_c|$ are the observed and calculated structure factor amplitudes, respectively. R_{free} is calculated using the same expression for reflections contained in the test set held aside during refinement.

[f] Calculated with MolProbity.